ADVANCED MATERIALS
www.advmat.de

A High-Energy Tellurium Redox-Amphoteric Conversion Cathode Chemistry for Aqueous Zinc Batteries

Jingwei Du, Yirong Zhao, Xingyuan Chu, Gang Wang, Christof Neumann, Hao Xu, Xiaodong Li, Markus Löffler, Qiongqiong Lu, Jiaxu Zhang, Dongqi Li, Jianxin Zou, Daria Mikhailova, Andrey Turchanin, Xinliang Feng, and Minghao Yu**

Rechargeable aqueous zinc batteries are potential candidates for sustainable energy storage systems at a grid scale, owing to their high safety and low cost. However, the existing cathode chemistries exhibit restricted energy density, which hinders their extensive applications. Here, a tellurium redox-amphoteric conversion cathode chemistry is presented for aqueous zinc batteries, which delivers a specific capacity of 1223.9 mAh g_{Te}^{-1} and a high energy density of 1028.0 Wh kg_{Te}^{-1}. A highly concentrated electrolyte (30 mol kg^{-1} $ZnCl_2$) is revealed crucial for initiating the Te redox-amphoteric conversion as it suppresses the H_2O reactivity and inhibits undesirable hydrolysis of the Te^{4+} product. By carrying out multiple operando/ex situ characterizations, the reversible six-electron $Te^{2-}/Te^0/Te^{4+}$ conversion with $TeCl_4$ is identified as the fully charged product and ZnTe as the fully discharged product. This finding not only enriches the conversion-type battery chemistries but also establishes a critical step in exploring redox-amphoteric materials for aqueous zinc batteries and beyond.

1. Introduction

Compared with non-aqueous batteries (e.g., lithium-ion batteries), aqueous batteries offer more viable prospects for grid energy storage, in which cost, safety, and sustainability are all crucial indexes.[1] Among the various aqueous battery options, aqueous zinc batteries (AZBs) assembled with mild aqueous electrolytes are the most appealing candidates owing to their favorable characteristic of directly using low-price, capacity-dense (820 mAh g^{-1}), and aqueous electrolyte-compatible (redox potential of −0.76 V vs standard hydrogen electrode) Zn metal anodes.[2] To advance the technology readiness level, significant efforts over the past few years have been devoted to overcoming Zn stripping/plating deficiencies, such as dendrite formation, electrolyte corrosion, and side reactions.[3] A variety of strategies has successfully tackled these problematic anode issues, ranging from current collector design[4] to interphase construction[3b,5] and electrolyte engineering.[3a,6] Impressively, ideal Zn stripping/plating chemistries that are dendrite-free, have close-to-unity coulombic efficiencies (>99.9%), and can cycle for an extremely long time (e.g., >500 cycles at 1 mAh cm^{-2})

J. Du, X. Chu, G. Wang, H. Xu, J. Zhang, D. Li, X. Feng, M. Yu
Faculty of Chemistry and Food Chemistry
Center for Advancing Electronics Dresden (cfaed)
Technische Universität Dresden
01062 Dresden, Germany
E-mail: xinliang.feng@tu-dresden.de; minghao.yu@tu-dresden.de

Y. Zhao, D. Mikhailova
Institute for Materials Chemistry
Leibniz Institute for Solid State and Materials Research (IFW) Dresden e.V.
Helmholtzstraße 20, 01069 Dresden, Germany

G. Wang
Key Laboratory of Advanced Fuel Cells and Electrolyzers Technology of Zhejiang Province
Ningbo Institute of Material Technology and Engineering
Chinese Academy of Sciences
Ningbo 315201, China

The ORCID identification number(s) for the author(s) of this article can be found under https://doi.org/10.1002/adma.202313621

DOI: 10.1002/adma.202313621

C. Neumann, A. Turchanin
Institute of Physical Chemistry and Center for Energy and Environmental Chemistry Jena (CEEC Jena)
Friedrich Schiller University Jena
Lessigstraße 10, 07743 Jena, Germany

H. Xu, J. Zou
Center of Hydrogen Science
State Key Laboratory of Metal Matrix Composites
School of Materials Science and Engineering
Shanghai Jiao Tong University
Shanghai 200240, China

X. Li, X. Feng
Department of Synthetic Materials and Functional Devices
Max Planck Institute of Microstructure Physics
Weinberg 2, 06120 Halle, Germany

M. Löffler
Dresden Center for Nanoanalysis (DCN)
Center for Advancing Electronics Dresden (cfaed)
Technische Universität Dresden
Helmholtzstraße 18, 01069 Dresden, Germany

Q. Lu
Institute of Materials
Henan Academy of Sciences
Zhengzhou 450046, China

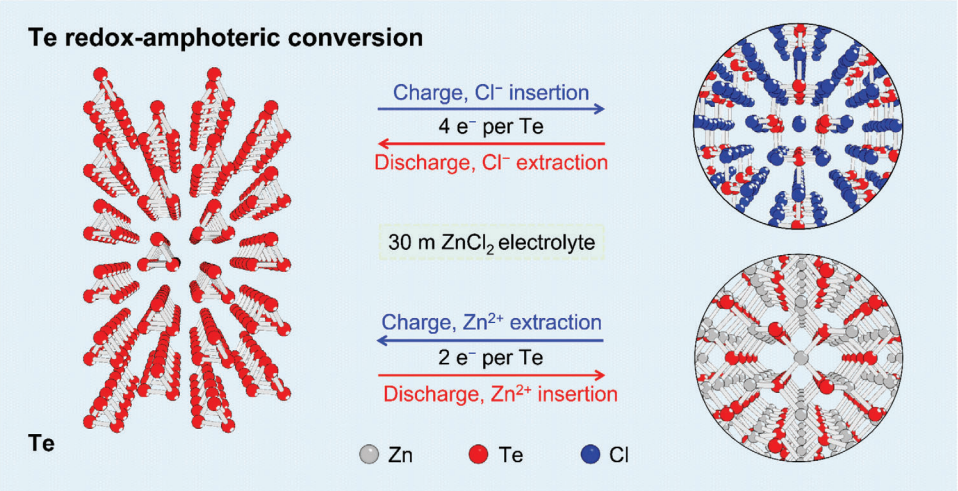

Figure 1. Schematic showing the Te redox–amphoteric conversion process. During the redox–amphoteric conversion, Te can be either oxidized to $TeCl_4$ or reduced to ZnTe.

even under harsh conditions (e.g., >5 mA cm^{-2}), have become ubiquitous in recent reports.[7]

To expand the application scope of AZBs, another pivotal priority is to further boost their energy densities. As Zn metal appears as an unshakable anode material, developing high-voltage, large-capacity cathode materials represents the most feasible approach to enhancing the energy density of AZBs.[8] Taking inspiration from lithium-ion battery cathodes, various materials with the cation-hosting (i.e., H^+ and Zn^{2+}) capability have been explored as the AZB cathodes. As high-energy representatives, intercalation-type Mn-based[9] and V-based[10] oxides exhibited high specific capacities (Q_S) in the range of ≈200–600 mAh g^{-1} and decent midpoint discharge voltage (V_{mid}) of ≈0.7–1.3 V versus Zn, presenting energy density ($E_{cathode} = Q_S \times V_{mid}$) of up to 420 Wh kg^{-1}. Coordination-type organic compounds with tailorable molecular structures (e.g., *para*-dinitrobenzene[11] and quinone)[12] also achieved high specific capacities of ≈400 mAh g^{-1} with relatively low midpoint discharge voltage (≈0.6–1.0 V vs Zn); thus, delivering energy density of ≈330 Wh kg^{-1}. Besides, recent studies demonstrated the use of high-capacity conversion-type cathode chemistries in Zn batteries, such as S (1148 mAh g^{-1}),[13] Se (611 mAh g^{-1}),[14] and Te (419 mAh g^{-1}).[15] However, restricted by their insufficient midpoint discharge voltage (0.63, 1.23, and 0.58 V versus Zn for S, Se, and Te, respectively), these conversion-type cathodes presented moderate energy densities up to 750 Wh kg^{-1}. Evidently, the most promising cathode design for the high-energy-density is to enable both a large specific capacity and high midpoint discharge voltage. In this respect, one hypothetical paradigm is to initiate additional Faradic reactions of established cathode materials at the high potential, which, however, seems to pose an insurmountable challenge.

Here, we further tackle the cathode limitation of AZBs by achieving an attractive Te redox-amphoteric conversion cathode chemistry (**Figure 1**), which delivers an ultra-large specific capacity (1223.9 mAh g_{Te}^{-1}) and a high energy density (1028.0 Wh kg_{Te}^{-1}). We discover that a highly concentrated electrolyte of 30 m (moles of salt per kg of solvent), $ZnCl_2$, plays a crucial role in enabling the reversible redox-amphoteric conversion by breaking the hydrogen-bonding network among H_2O and inhibiting the H_2O reactivity toward the Te^{4+} hydrolysis. Through electrochemical investigation and multiple characterizations, we reveal the successful six-electron $Te^{2-}/Te^0/Te^{4+}$ conversion with Cl^- and Zn^{2+} as the charge carrier ions for the fully charged and discharged products, respectively. The overall Faradic reactions associated with the Te conversion are proposed as Equations (1) and (2). The distinctive charge-storage characteristics of the Te redox-amphoteric conversion chemistry offer promising opportunities for developing advanced AZBs for high-energy purposes.

$$Te + 4Cl^- \leftrightarrow TeCl_4 + 4e^- \quad (1)$$

$$Te + Zn^{2+} + 2e^- \leftrightarrow ZnTe \quad (2)$$

2. Results and Discussion

2.1. Enabling Reversible Te Redox-Amphoteric Conversion Chemistry

Elemental Te was selected as the cathode material due to its metalloid feature with compromised properties of metal and nonmetal. Te with a strong electron affinity (−190.2 kJ mol^{-1} for the first electron affinity) can accommodate metal cations and be converted into metal tellurides. This conversion chemistry has been widely taken for the cathodes of various batteries, including AZBs with $ZnTe_2$ and ZnTe formed in sequence.[15] On the other hand, Te exhibits metal-like properties with low ionization energies (869.3 kJ mol^{-1} for the first ionization energy), allowing it to lose electrons and form cationic Te easily. In particular, the standard Te^{4+}/Te potential (0.57 V vs standard hydrogen electrode) is 1.33 V higher than the standard Zn^{2+}/Zn potential, which indicates the high promise to extend the Te^{4+}/Te redox couple to the Te cathode of AZBs. However, the attractive Te^{4+}/Te redox couple has not been achieved in aqueous batteries, which, we speculate, comes from two challenging factors: 1) the

strong hydrolysis of the formed Te^{4+} salts, which induces an irreversible conversion reaction[16] and 2) the need for proper charge-compensated anions, which determine the realistic reaction thermodynamics and kinetics. Our hypotheses find support in the latest study,[17] where reversible Te^{2-}/Te^{4+} conversion was realized using a non-aqueous ionic-liquid electrolyte system (i.e., 1-butyl-3-methylimidazolium chloride/ethylene glycol/$ZnCl_2$). This electrolyte, with its broad voltage window and highly nucleophilic Cl^- anions, initiated the Te^{4+}/Te conversion, resulting in a high specific capacity of 654.2 mAh g_{Te}^{-1} for the Te electrode.

With due consideration of the above analysis, we first evaluated the Te conversion chemistry in a two-electrode cell with a Zn foil anode and a ball-milled Te-graphite cathode (denoted TeG). Ball-milling with graphite represents a trivial approach for electrode preparation, which ensures the creation of a superior conductive matrix capable of accommodating active materials with large volume changes. After ball-milling, TeG displayed a homogeneous distribution of Te and graphite (Figure S1, Supporting Information), demonstrating a high Te mass ratio of 53% (Figure S2, Supporting Information). Characteristic Te peaks could still be observed in the XRD pattern of TeG (Figure S3, Supporting Information). A 30 M $ZnCl_2$ aqueous electrolyte was specially chosen because the H_2O molecules in it were completely coordinated to Zn^{2+} or Zn–Cl complexes as ligands,[18] showing considerably restricted motion capability. Thereby, the H_2O reactivity could be minimized; thus, inhibiting unwanted hydrolysis of the Te^{4+} salt. Moreover, 30 M $ZnCl_2$ showed facile Zn stripping/plating, which enabled a dendrite-free Zn metal anode without the formation of solid electrolyte interphase.[19]

We evaluated the anodic stability of 30 M $ZnCl_2$ using linear sweep voltammetry in a two-electrode Swagelok cell with titanium foil as the working electrode. As shown in Figure S4, Supporting Information, the electrolyte demonstrated remarkable anodic stability beyond 2 V. In addition, we anticipated that small and single-atom Cl^- ions could dissociate from the Zn–Cl complexes and act as charge carriers to participate in the Te^{4+}/Te redox reaction. To our delight, successful Te redox-amphoteric conversion was achieved, as supported by the cyclic voltammetry (CV) curves (Figure S5, Supporting Information) and the first three-cycle galvanostatic charge/discharge (GCD) curves of TeG (Figure S6a, Supporting Information). An ultrahigh-specific capacity of 1082.2 mAh g_{Te}^{-1} at 400 mA g_{Te}^{-1} was achieved by TeG. Nevertheless, we also noticed rapid capacity decay of TeG with a specific capacity of 493.5 mAh g_{Te}^{-1} retained after only 14 cycles (Figure S6b, Supporting Information). This capacity decay could originate from the quick loss of active material as we discovered the high solubility of $TeCl_4$ in 30 M $ZnCl_2$ (up to 1.7 M at room temperature, Figure S7, Supporting Information). Besides, consumption of Cl^- anions in the 30 M $ZnCl_2$ electrolyte leads to a change in the local electrolyte environment, causing the irreversible hydrolysis of Te^{4+}.

The encouraging Te redox-amphoteric conversion motivated us to address the solubility issue by replacing the electrolyte with a hydrogel one made up of 30 M $ZnCl_2$ and polyethylene oxide (Figure S8, Supporting Information). As shown in **Figure 2a**, the first-cycle GCD profile of TeG measured in the hydrogel electrolyte was almost identical to that measured in 30 M $ZnCl_2$; while the reversibility was substantially improved in the following two cycles. During the beginning charge cycle, TeG underwent a conditioning process with a specific charge capacity of 901.7 mAh g_{Te}^{-1}, indicating a roughly four-electron transfer per Te atom. The charge plateau was clearly higher than the following charge cycles, as Te within TeG began in an ordered crystalline phase with a trigonal structure. The conversion reaction in the first charge cycle experienced considerable polarization owing to the sluggish kinetics of chloridizing Te with a large domain size.[37] A similar conclusion could be confirmed through the galvanostatic intermittent titration technique (GITT) measurement performed on the TeG electrode (Figure S9, Supporting Information). The TeG electrode exhibited apparently smaller ion diffusion coefficients during the initial charge cycle ($\approx 1.2 \times 10^{-14}$–$1.1 \times 10^{-12}$), compared with the subsequent charge/discharge cycles ($\approx 4.5 \times 10^{-14}$–$4.6 \times 10^{-10}$). Subsequently, TeG depicted nearly identical charge–discharge profiles with a highly reversible discharge capacity of 1223.5 mAh g_{Te}^{-1}, corresponding to ≈5.8-electron transfer per Te atom. It is worth noting that the discharge curve could be divided into two distinct voltage ranges, that is, a plateau at ≈1.27–0.80 V versus Zn and a slope at ≈0.80–0.10 V versus Zn. This observation agrees well with the two Faradic reaction regions observed in the CV profile of TeG (Figure 2b). The two charge-storage regions dominantly came from the redox-amphoteric conversion of Te, which could be supported by the collected CV curves of TeG and ball-milled graphite (Figure S10, Supporting Information). The capacity contribution of graphite in TeG was determined negligible (<1.5%). Compared with bulk Te, TeG showed a CV curve with a much larger current density, which indicates the boosted charge-storage kinetics enabled by graphite (Figure S11, Supporting Information).

All the above results imply that the attractive six-electron conversion chemistry for Te (i.e., $Te^{2-}/Te^0/Te^{4+}$) has been achieved. The Te redox-amphoteric conversion chemistry allows for an ultrahigh energy density of 1028.0 Wh kg_{Te}^{-1}, which is at least two times higher than the energy densities of the reported intercalation-type Mn-/V-based oxides, organic compounds, polyanion compounds, Prussian blue analogs, as well as other reported conversion-type chemistries (Figure 2c; Table S1, Supporting Information). The Te/Te^{4+} conversion accounted for 86.7% of the total energy density (Figure S12, Supporting Information). We further calculated the energy density based on the overall battery reaction, as shown in Equation (3), which notably reached 287.9 Wh kg^{-1}. This value still stands as the state-of-the art in comparison with recently reported AZBs (Figure 2d), such as Zn//α-MnO_2 (271.0 Wh kg^{-1}),[9b] Zn//$CoFe(CN)_6$ (250.1 Wh kg^{-1}),[36] Zn//$Zn_{0.3}V_2O_5{\cdot}1.5\ H_2O$ (243.8 Wh kg^{-1}),[10a] Zn//Calix[4]quinone (220.0 Wh kg^{-1}),[12] and Zn//$VOPO_4$ (185.5 Wh kg^{-1}).[32] Moreover, GCD profiles at various current densities were also collected to assess the rate capability of TeG (Figure S13, Supporting Information). Notably, the TeG electrode maintained a consistent shape as the current density escalated from 0.4 to 1.0 A g_{Te}^{-1}, achieving a high specific capacity of 901.0 mAh g_{Te}^{-1} at 1.0 A g_{Te}^{-1}.

Further, the six-electron Te conversion chemistry exhibits decent cycling stability in the hydrogel electrolyte (Figure 2d). The specific capacity gradually increases during the initial cycling process. These initial cycles typically enhance electrode wettability with the electrolyte and facilitate ion transport at the electrode/electrolyte interface, which contributes to promoting electrochemical conversion efficiency and increasing the specific

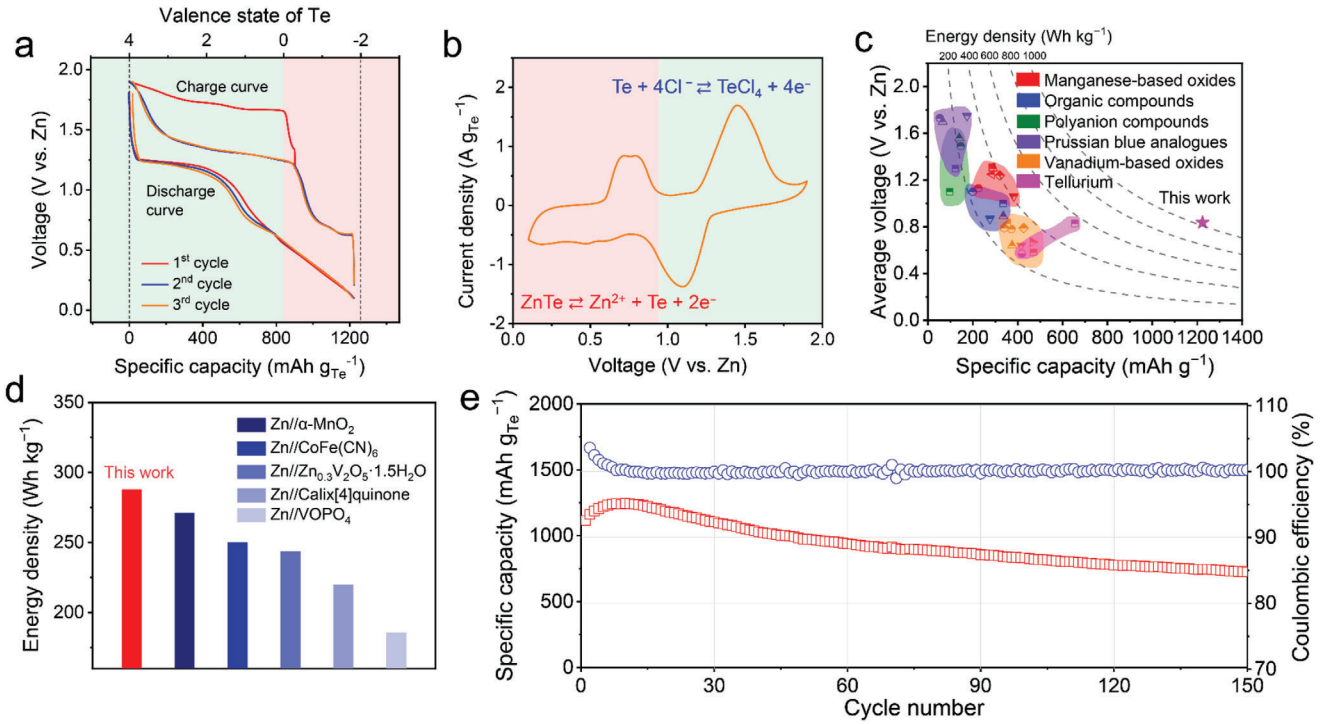

Figure 2. Performance of the Te redox–amphoteric conversion chemistry. a) The initial three-cycle GCD profiles of TeG at 400 mA g_{Te}^{-1}. b) CV curve of TeG at 0.2 mV s^{-1}. c) Performance comparison (including gravimetric capacity, midpoint discharge voltage, and gravimetric energy density) of Te conversion chemistry with reported AZB cathode chemistries, such as intercalation-type Mn-/V-based oxides (γ-MnO2,[20] β-MnO2,[21] α-MnO2-graphene scrolls,[22] K0.8Mn8O16,[23] α-MnO2,[9b] Zn0.3V2O5·1.5H2O,[10a] V2O5,[24] VO2,[25] and V3O7·H2O),[26] organic compounds (calix[4]quinone,[12] polyaniline,[27] pyrene-4,5,9,10-tetraone,[28] and HqTp COF),[29] polyanion compounds (Na3V2(PO4)3,[30] Li3V(PO4)3,[31] and VOPO4),[32] Prussian blue analogues (FeFe(CN)6,[33] CuFe(CN)6,[34] Zn3[Fe(CN)6]2,[35] and CoFe(CN)6),[36] and tellurium.[15,17] d) Energy density comparison of the Zn//Te device with recently reported AZB devices. The energy density was calculated based on the overall battery reaction, including active anode, cathode materials, as well as the consumed electrolyte salt. e) Cycling performance of TeG at 400 mA g_{Te}^{-1}.

capacity. After 150 charge/discharge cycles at 400 mA g_{Te}^{-1}, TeG still maintains a high specific capacity of 725.7 mAh g_{Te}^{-1}. In the cycling test at 1.5 A g_{Te}^{-1} (Figure S14, Supporting Information), TeG maintains a specific capacity of 382 mAh g_{Te}^{-1} after 300 charge/discharge cycles with the capacity retention of 65%.

$$ZnTe + 2ZnCl_2 \leftrightarrow TeCl_4 + 3\ Zn \quad (3)$$

2.2. The Crucial Role of the Highly Concentrated Electrolyte

It is intriguing to observe that the reversible Te redox-amphoteric conversion, particularly the reversible Te^0/Te^{4+} redox couple, can be achieved only in the highly concentrated 30 M $ZnCl_2$ electrolyte, but not in the diluted $ZnCl_2$ electrolytes. To elucidate the role of the highly concentrated electrolyte in initiating the reversible six-electron conversion of Te, we compared the electrochemical performance of TeG in the $ZnCl_2$ electrolytes with varying concentrations (1, 15, and 30 M). It is notable that the conditioning process in the beginning charge cycle was observed for TeG in all three electrolytes (Figure S15, Supporting Information), indicating the Te^0/Te^{4+} conversion. However, TeG behaved differently from the following discharge cycle. The GCD curves of TeG after conditioning in different electrolytes are presented in **Figure 3a**. In 1 M $ZnCl_2$, TeG displayed a huge charge–discharge polarization (0.71 V at mid-capacity) with a small reversible capacity of 411 mAh g_{Te}^{-1}. By contrast, the charge–discharge polarization of TeG was only 0.39 V in 30 M $ZnCl_2$, close to that in the hydrogel electrolyte (0.36 V). TeG in 15 M $ZnCl_2$ behaved as an intermediate between 1 M $ZnCl_2$ and 30 M $ZnCl_2$. The same conclusion could also be drawn by comparing the CV curves of TeG in different electrolytes (Figure 3b; Figure S16, Supporting Information).

To investigate the conversion products of TeG in 1 M $ZnCl_2$ and 30 M $ZnCl_2$, we conducted the X-ray diffraction (XRD) analysis on TeG at different charge/discharge states (Figure S17, Supporting Information). The XRD spectra showed clear characteristic peaks of TeO_2 for the fully charged TeG electrode in 1 M $ZnCl_2$, but no obvious XRD peaks could be detected for the fully charged TeG electrode in 30 M $ZnCl_2$. This result unveils that Te in TeG was electrochemically oxidized into TeO_2 in 1 M $ZnCl_2$, and the involvement of the electrolyte H_2O was deduced through Equations (4) and (5). Our conclusion is also supported by the drastic hydrolysis of $TeCl_4$ to produce TeO_2 (Figure 3c; Figure S18, Supporting Information), which demonstrates that $TeCl_4$ cannot stably exist in 1 M $ZnCl_2$. In contrast, no hydrolysis reaction was observed for $TeCl_4$ in 30 M $ZnCl_2$ (Figure 3d). Moreover, the CV curves of the commercial TeO_2 were collected in 30 M $ZnCl_2$ (Figure S19, Supporting Information), showing a completely different shape from the CV curves of TeG. This finding further

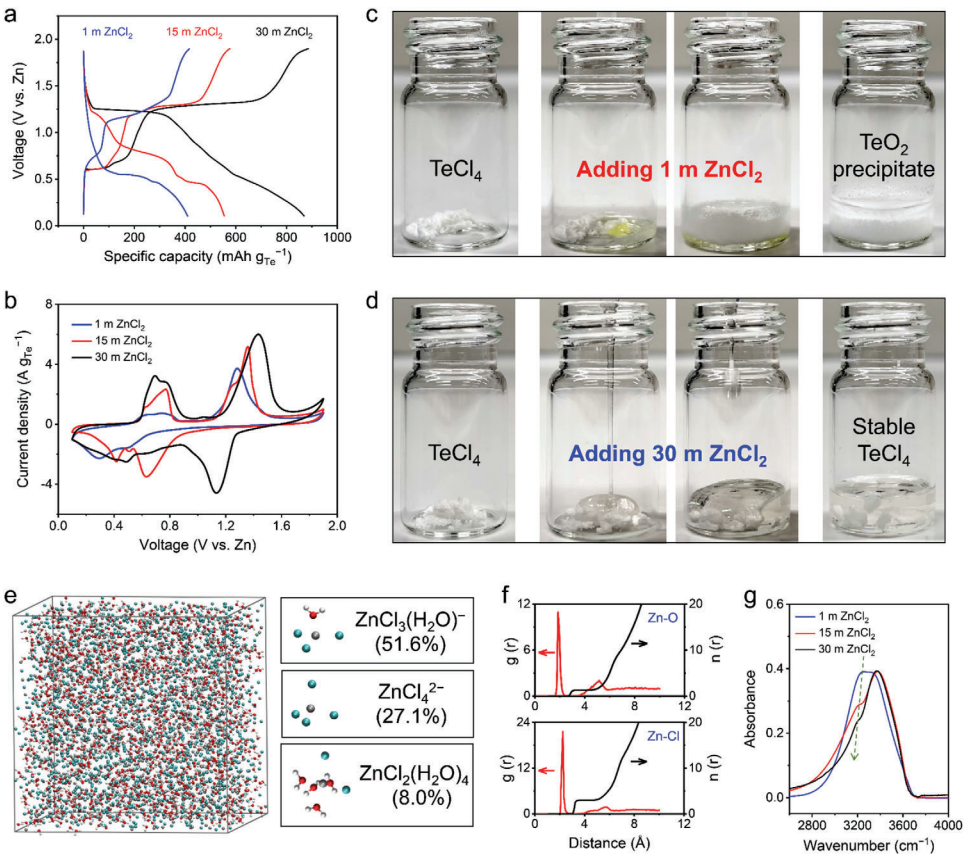

Figure 3. Te conversion chemistries in different electrolytes. a) GCD curves at 400 mA g_{Te}^{-1} and b) CV curves at 1 mV s^{-1} of TeG in the $ZnCl_2$ electrolytes with different concentrations. c,d) Optical photos of adding 1 M $ZnCl_2$ (c) and 30 M $ZnCl_2$ into commercial $TeCl_4$ (d). e) Snapshot of the 30 M $ZnCl_2$ electrolyte and the typical local coordination structures of Zn in the molecular dynamics simulation. White atoms, red atoms, cyan atoms, and gray atoms are H, O, Cl, and Zn atoms, respectively. f) Radial distribution functions g(*r*) and integral profiles n(r) of Zn–O (of H_2O) and Zn–Cl coordination in 30 M $ZnCl_2$. g) FTIR spectra of the $ZnCl_2$ electrolytes with different concentrations.

confirms the absence of unwanted TeO_2 in TeG after conditioning in 30 M $ZnCl_2$.

$$Te \rightarrow Te^{4+} + 4e^- \quad (4)$$

$$Te^{4+} + 2H_2O \rightarrow TeO_2 + 4H^+ \quad (5)$$

Molecular dynamics simulations provide further insights into the strong resistance of the 30 M $ZnCl_2$ electrolyte toward the hydrolysis of $TeCl_4$. In 1 M $ZnCl_2$ (Figure S20, Supporting Information), Zn^{2+} ions are surrounded by abundant water molecules, and the typical coordination configurations of Zn^{2+} have hydration numbers of 5 (40.3%) and 6 (58.3%). The first-shell coordination ligands of Zn^{2+} are 5.47 O (of H_2O) and 0.45 Cl on average, as determined by the radial distribution function (g(*r*)) spectra. When the $ZnCl_2$ concentration increases to 30 M (Figure 3e), dominant Zn^{2+} configurations exhibit hydration numbers of 0 (27.1%), 1 (51.6%), and 4 (8%). The average first-shell Zn–O (i.e., Zn—H_2O) and Zn—Cl coordination numbers become 1.34 and 3.10 (Figure 3f). These unique Zn^{2+} coordination configurations in 30 M $ZnCl_2$ break the hydrogen-bonding network among H_2O, which is also evidenced by the considerably weakened intensity of the H-bonded O—H content (3205−3370 cm^{-1}) in the Fourier-transform infrared (FTIR) spectrum of 30 M $ZnCl_2$ (Figure 3g).[38] Thereby, H_2O molecules are mostly restricted in the first coordination shell of Zn^{2+}, showing inert reactivity to hydrolyze Te^{4+}.

2.3. Mechanism Elucidation

We next focused on revealing the redox-amphoteric conversion mechanism of TeG in 30 M $ZnCl_2$. X-ray photoelectron spectroscopy (XPS) was first measured for TeG at different charge/discharge states. Of note, XPS is a surface-sensitive spectroscopic technique with a probe depth of a few nm. In the Te 3d XPS (**Figure 4a**), Te^{4+} signals were detected for all samples because the surface of ball-milled Te oxidizes quickly upon exposure to air.[39] Apart from the Te^{4+} peaks, we found two additional peaks at 573.5 and 583.9 eV for pristine TeG, corresponding to elemental Te (i.e., Te^0-graphite) $3d_{5/2}$ and $3d_{3/2}$ peaks. The slightly higher binding energy of the Te^0-graphite peaks in the pristine TeG electrode compared with standard Te^0 peaks could be attributed to the ball-milling fabrication of TeG, a process that triggered the formation of interfacial Te—C bonds and induced electron transfer from Te to C. After charging to 1.9 V, the Te^0 peaks nearly vanished; while the Te^{4+} peaks were notably

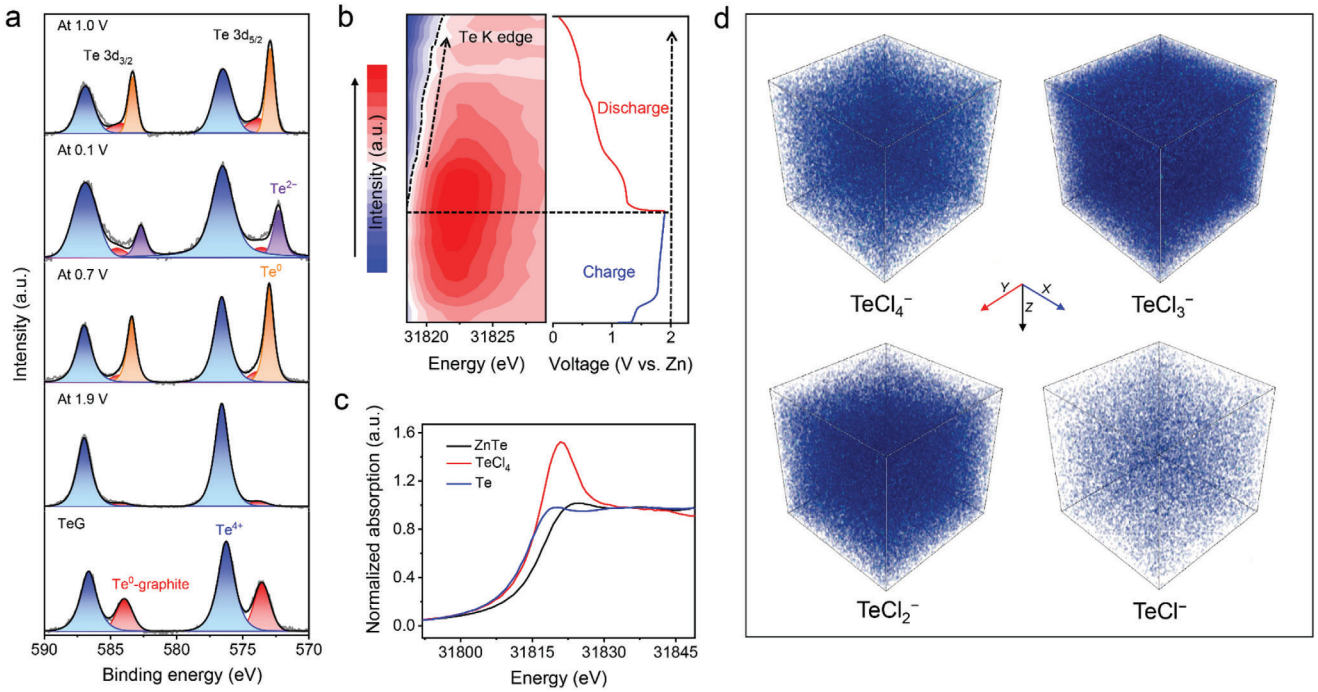

Figure 4. Spectroscopic analysis of TeG at different charge–discharge stages. a) Te 3d XPS spectra of TeG at different charge/discharge states. b) Operando Te K-edge XANES spectra in the contour map (left) during the initial charge/discharge process (right). c) Te K-edge XANES spectra of ZnTe, $TeCl_4$, and Te references. d) The TOF-SIMS 3D reconstruction of the $TeCl_4^-$, $TeCl_3^-$, $TeCl_2^-$, and $TeCl^-$ signals.

enhanced, indicating complete Te^0/Te^{4+} conversion. The Te^0 peaks reappeared when TeG was discharged to 0.7 V, and they shifted to 572.2 (Te $3d_{5/2}$) and 582.6 eV (Te $3d_{3/2}$), respectively, at 0.1 V, reflecting the formation of Te^{2-}. During the subsequent charge to 1.0 V, Te^{2-} was again converted to Te^0, confirming the reversible $Te^{2-}/Te^0/Te^{4+}$ conversion chemistry. We also noticed the potential existence of an intermediate state between Te^0 and Te^{4+} (such as Te^{2+}),[17] which was hinted at by the detection of two split reduction peaks in the CV curves of bulk Te at ≈0.8–1.3 V (Figure S11, Supporting Information). However, experimental confirmation of this intermediate appeared challenging due to the metastability of such a state (Figures S2 and 22, Supporting Information). Besides, Zn 2p XPS spectra indicated an intensive signal at 1022.3 eV for TeG at 0.1 V, suggesting the involvement of Zn^{2+} in the fully discharged product (Figure S23, Supporting Information).

Operando synchrotron X-ray absorption spectroscopy (XAS) was implemented to monitor the local chemical environment evolution of Te in TeG during the initial charge/discharge cycle. Figure 4b displays the operando Te K-edge X-ray absorption near-edge structure (XANES) spectra of TeG. Meanwhile, the Te, ZnTe, and $TeCl_4$ references were also measured for comparison and analysis (Figure 4c). During the initial charge process, an adsorption peak at 31 823 eV gradually appeared, in good agreement with the characteristic peak of $TeCl_4$. The peak evolution trend agreed with the spectrum change from the Te reference to the $TeCl_4$ reference, implying that $TeCl_4$ is the charging product. This conclusion was also supported by the analysis of TeG at the fully charged state using time-of-flight secondary ion mass spectrometry (TOF-SIMS, Figure S24, Supporting Information). The 3D reconstruction of TOF-SIMS signals (Figure 4d) clearly demonstrated the uniform distribution of Te—Cl species (i.e., $TeCl_4^-$, $TeCl_3^-$, $TeCl_2^-$, and $TeCl^-$) throughout the bulk electrode. In addition, the Te K-edge XANES peak at 31 823 eV diminished progressively during the discharge cycle (Figure 4b), indicating the reduction of Te^{4+} to Te^0. As the discharge progressed, the absorption edge underwent a blue shift, consistent with the spectrum change from the Te reference to the ZnTe reference. Meanwhile, the presence of crystalline ZnTe in the high-resolution transmission electron microscopy image of TeG at the fully discharged state (Figure S25, Supporting Information) further confirmed ZnTe as the discharged product.

Further, we extracted the extended X-ray absorption fine structure (EXAFS) of TeG at the fully charged (1.9 V) and fully discharged (0.1 V) states. In order to distinguish the backscattering atoms of Te, the wavelet transform (WT) analysis on the k^3-weighted EXAFS data with a 2D representation in R and k spaces was performed. As revealed, initial TeG (**Figure 5**a) exhibited the WT maxima position at R = 2.52 Å, which refers to the Te—Te scattering. A new signal appeared at R = 1.99 Å of TeG at 1.9 V, corresponding to Te—Cl scattering (Figure 5b). The change trend between initial TeG and TeG at 1.9 V was consistent with WT maxima position change from the Te reference to the $TeCl_4$ reference (Figure S26a,b, Supporting Information). Of note, the signal at R = 1.4 Å was attributed to the scattering path with O atoms, which could also be identified in initial TeG. The presence of the Te-O scattering could be explained by the slight surface oxidation of TeG. WT maxima of TeG at 0.1 V was ≈R = 2.21 Å, indicating a possible Te—Zn path in TeG at 0.1 V (Figure 5c). The changing trend of objective signals followed the spectra evolution from the

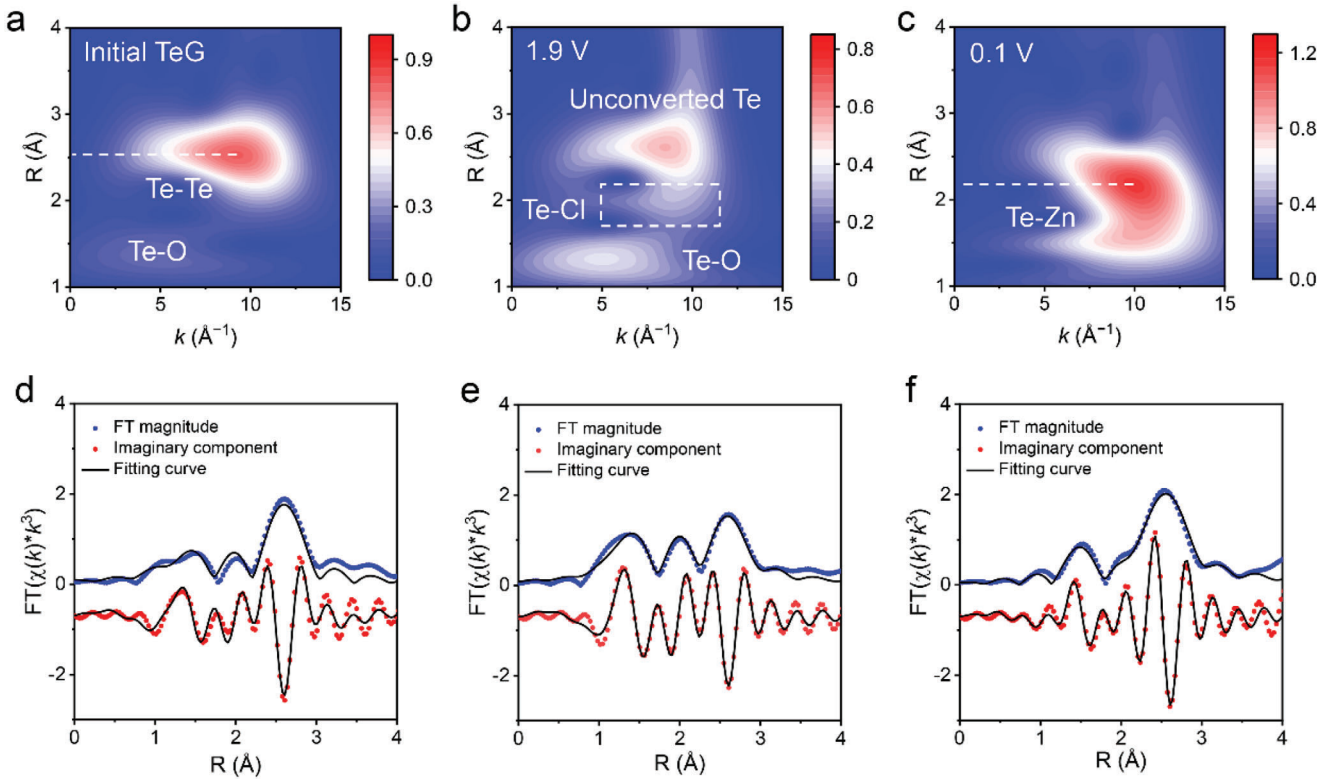

Figure 5. The EXAFS analysis of TeG at different states. Wavelet-transformed Te K-edge EXAFS of a) initial TeG, b) fully charged TeG (1.9 V), and c) fully discharged TeG (0.1 V). EXAFS data (points) and fit curve (line) in R-space (Fourier transform [FT] magnitude and imaginary component) for d) initial TeG, e) fully charged TeG (1.9 V), and f) fully discharged TeG (0.1 V). The data are k3-weighted without phase correction.

$TeCl_4$ reference to the ZnTe reference (Figure S26b,c, Supporting Information).

Based on the WT analysis, EXAFS fitting was further carried out with different coordination paths (Table S3, Supporting Information). A reference sample of ZnTe was utilized to determine the amplitude reduction factor (S_0^2, 0.89), which is an experiment-related constant (Figure S27 and Table S2, Supporting Information). At the initial state (*R*-space in Figure 5d; *k*-space in Figure S28a, Supporting Information), the EXAFS result was fitted with two coordination paths, namely Te—O as in crystalline TeO_2 (space group: $P2_12_12_1$) and Te—Te as in crystalline elemental Te (space group: $P3_121$). The coordination number (*N*) of the Te—O path (surface oxidation species) and Te—Te path was 0.8 ± 0.3, and 2, respectively. At the fully charged state (1.9 V), the EXAFS spectrum (Figure 5e; Figure S28b, Supporting Information) was well fitted with three coordination paths, including Te—O as in crystalline TeO_2, Te—Cl as in crystalline $TeCl_4$ (space group: $C2/c$), and Te—Te as in crystalline elemental Te. The Te—Te (N = 0.8 ± 0.2) path could come from the partially unconverted Te in TeG. The Te—O path could be attributed to the original surface oxidation and partial hydrolysis of Te^{4+} due to the local electrolyte environment change. Importantly, the Te—Cl path with N = 3 matched well with $TeCl_4$, signifying $TeCl_4$ as the fully charged product of TeG in 30 M $ZnCl_2$. Besides, the EXAFS spectrum at the fully discharged state (0.1 V) was fitted with the Te—Zn path (as in crystalline ZnTe, space group, $F\bar{4}3m$, N = 2), Te—O path (N = 0.3 ± 0.2), and Te—Te path (N = 1.1 ± 0.4), corresponding to ZnTe as the fully discharged product, surface oxidation species, and unconverted Te, respectively (Figure 5f; Figure S28c, Supporting Information).

In addition, we carried out ex situ Raman spectra of TeG (Figure S29, Supporting Information), which further support our proposed ZnTe/Te/$TeCl_4$ conversion mechanism in 30 M $ZnCl_2$ and highlight the inhibition of Te^{4+} hydrolysis. As additional evidence, we measured the CV curves of commercial ZnTe and $TeCl_4$ in 30 M $ZnCl_2$ (Figure S30, Supporting Information). As expected, both ZnTe and $TeCl_4$ present a similar CV shape with TeG after the first-cycle conditioning. All these findings collectively prove the six-electron Te redox-amphoteric conversion in 30 M $ZnCl_2$, as expressed in Equations (1) and (2).

3. Conclusion

In conclusion, we have demonstrated a reversible Te redox-amphoteric conversion cathode chemistry for AZBs, which exhibited an exceptionally high specific capacity of 1223.9 mAh g_{Te}^{-1} and a large energy density of 1028.0 Wh kg_{Te}^{-1}. The six-electron $Te^{2-}/Te^0/Te^{4+}$ conversion chemistry was achieved in a highly concentrated $ZnCl_2$ electrolyte, which effectively inhibited the hydrolysis of the Te^{4+} product. Through electrochemical and spectroscopic analysis, we disclosed that small-size Cl^- served as important charge carriers to participate in the reversible Te^0/Te^{4+} conversion, and the overall redox-amphoteric conversion reaction was demonstrated as the ZnTe/Te/$TeCl_4$ conversion. The

proposed redox-amphoteric conversion mechanism represents a novel paradigm for pursuing new battery chemistries with high energy density.

The remarkably high specific energy density offers exciting potential for the practical use of the reported Te conversion chemistry in various real-world energy storage applications, presenting a safe and high-energy solution. However, we acknowledge that the limited abundance (annual production: 580 tons in 2021) and high cost (71$ per kg) of the raw material could impose constraints on its widespread adoption, especially in applications demanding affordability and scalability. In our exploration, we also discovered that elemental Se, which is significantly more abundant (annual production: 3000 tons in 2020) and cost-effective (17.6$ per kg) than Te could undergo a similar reversible redox-amphoteric conversion reaction in the 30 M $ZnCl_2$-based hydrogel electrolyte (Figure S31, Supporting Information). The reversible six-electron reaction delivered an extremely high specific capacity of 1914.3 mAh g_{Se}^{-1}, resulting in a highly attractive energy density of 1684.1 Wh kg_{Se}^{-1}. However, the Se conversion exhibited a much faster capacity decay than the Te conversion chemistry, retaining only 583.7 mAh g_{Se}^{-1} after ten cycles at 400 mA g_{Se}^{-1} in the hydrogel electrolyte. We speculate that the low durability of the Se conversion chemistry was attributed to the high reactivity toward H_2O; hence, more rational electrolytes (e.g., H_2O-free) will be needed to stabilize the Se conversion chemistry. Given the promising specific capacity and energy density, it is crucial to invest significant efforts in achieving the reversible and long-lasting $Se^{2-}/Se^0/Se^{4+}$ conversion for battery applications. Furthermore, there remains still significant space for further optimizing the electrode and electrolyte for both Te and Se conversion chemistries, aiming to enhance the active material ratio, rate performance, conversion kinetics, as well as cycling stability. We hope our presented results will attract extensive attention to working in this direction.

4. Experimental Section

Chemicals: Tellurium (Te, 99.8%), tellurium dioxide (TeO_2, ≥99%), tellurium tetrachloride ($TeCl_4$, 99%), zinc telluride (ZnTe, 99.99%), selenium (Se, ≥99.5%), zinc chloride ($ZnCl_2$, ≥98%), graphite (average size: 20 µm), poly(vinylidene fluoride) (PVDF; weight-average molecule weight, $M_w \approx$ 275 000), poly(ethylene oxide) (PEO, viscosity-average molecular weight, $M_v \approx$ 600 000), glass fiber membrane (0.42 mm thickness, 0.7 µm pore size), super P, *N*-Methyl-2-pyrrolidone (NMP, ≥99.8%), and Zn foil were purchased from Sigma–Aldrich. Graphene oxide (GO) was purchased from GaoxiTech Co., Ltd. Carbon cloth (thickness: 406 µm) was purchased from The Fuel Cell Store. All chemicals were directly used without further purification.

Preparation of TeG: TeG was synthesized by the high-energy ball-milling method. Specifically, 1.2 g tellurium and 0.8 g graphite were added in a stainless steel jar with stainless steel balls (mass ratio between mixed materials and balls: 1/20) in glove box with argon filling. The jar was transformed into a planetary micro-mill machine (PULVERISETTE 7, Fritsch GmbH) and ball-milled for 48 h at the rotation rate of 550 rpm. The TeG composite was then obtained and sealed in argon atmosphere for further investigation. The weight ratio of Te in TeG was measured to be 53.0% by thermogravimetric analysis.

Preparation of the Hydrogel Electrolyte: The highly concentrated $ZnCl_2$ electrolyte was first prepared by dissolving 30 M $ZnCl_2$ in deionized water. The gel electrolyte was prepared by blending 10 wt% PEO to 30 M $ZnCl_2$ and stirring the mixture overnight to ensure homogeneity. Afterward, a glass fiber membrane with a diameter of 10 mm was immersed in the gel electrolyte at 80 °C overnight. Finally, the membrane was taken out, placed onto a smooth glass substrate, and heated at 80 °C for 6 h to obtain the quasi-solid electrolyte.

Electrochemical Measurements: To prepare the TeG electrode, TeG, PVDF (binder), and super P were dispersed in NMP with a mass ratio of 8:1:1 and mixed homogeneously. The slurry was coated on carbon cloth, followed by drying in a vacuum oven at 80 °C for 12 h. Both anode and cathode were punched into round pellets with a diameter of 6 mm. The mass loading of active Te was about ≈1–1.5 mg cm^{-2}. Titanium rods and stainless-steel rods were used as current collectors for the cathode and anode, respectively, with a diameter of 10 mm. Commercial Whatman glass fiber membrane (Grade GF/D, thickness: 0.42 mm, pore size: 0.7 µm) was employed as the separator. For the cycling test, a graphene oxide (GO)-decorated glass fiber membrane was used as the separator. GO nanoflakes have found extensive use in modifying battery separators, effectively addressing the shuttling issue common in conversion-type cathodes. The polarized functional groups densely present on the GO surface can efficiently adsorb soluble Te-species, mitigating rapid capacity decay resulting from active material loss. Specifically, GO with an average lateral size of 20 µm was first mixed with deionized water to obtain GO aqueous solution with a concentration of 4 mg mL^{-1}. Then, 5 mL of GO solution was filtered by glass microfiber filters with a diameter of 47 mm. After drying in a vacuum oven overnight, the GO separators were cut into proper size for use. The batteries were assembled in Swagelok cells with Zn foil as the anode.

To assemble Zn//ZnTe and Zn//TeO_2 cells, commercial ZnTe or TeO_2, PVDF, and super P with a mass ratio of 7:2:1 were dispersed in NMP and mixed homogeneously. The battery assembly was the same as Zn//Te cells. As for Zn//$TeCl_4$ cells, commercial $TeCl_4$ and super P with a mass ratio of 9:1 were mixed homogeneously without solvent and directly pressed to titanium metal mesh (100 mesh) with a mass loading of ≈6 mg cm^{-2}. The battery assembly was also the same as Zn//Te cells in a glovebox.

CV curves were collected from CHI760E (CH Instruments) electrochemical workstation. GCD measurements were performed from a Land battery test system (LAND CT2001A) at 25 °C. Energy density (E) was calculated based on the GCD profile by Equation (6), where I is the applied current density based on the mass of Te, U is the cell output voltage, and t is the discharging time. Subsequently, the average voltage was derived by dividing the calculated energy density by the specific capacity as Equation (7).

$$E = I\int_0^t U(t)\,dt \tag{6}$$

$$\bar{U} = E/Q \tag{7}$$

Characterization: The morphologies and compositions of materials were studied by field-emission scanning electron microscope (SEM, Carl Zeiss Gemini 500), transmission electron microscopy (TEM, FEI Tecnai G^2 F30), X-ray diffraction (XRD, Bruker D8) applying Cu Kα radiation (λ = 0.154 nm), and thermogravimetric analysis (TGA, Netzsch DSC-204 F1). Infrared spectra were measured on an FT-IR Spectrometer Tensor II (Bruker) with an attenuated total reflection unit. X-ray photoelectron spectroscopy (XPS) was studied in an UHV multiprobe system (Scienta Omicron) with an Al K_α X-ray source and an electron analyzed (Argus CU) with 0.6 eV resolution. The spectra were calibrated using the C 1s peak (284.6 eV) and fitted using Voigt functions. The TOF-SIMS measurements were implemented by ION-TOF (GmbH, Germany) TOF-SIMS 5 with a bismuth ion source. Raman spectra were recorded with a Bruker RFS 100/S spectrometer at a wavelength of 532 nm.

Operando XAS measurements were conducted at beamline P65 from DESY. The measurements were performed at the K edge of Te (31.7–31.9 keV). A Si (311) crystal monochromator was used with a focused beam size of ≈0.5 × 1 mm^2 (vertical × horizontal). The data were

acquired in transmission mode at room temperature. For energy calibration, Te standard diluted to 20 wt% with cellulose was placed after the transmission chamber to align each measurement, and the energy calibration was conducted using the first-derivative point of XANES of Te. XAS data were processed and analyzed using the Demeter software package.[40] The XANES and EXAFS spectra were calibrated, normalized, and aligned by using Athena.[40,41] Quantitative curve fittings were done by using Artemis.[40] All scattering paths used for EXAFS fittings were taken from crystalline data and calculated by the free energy force field (FEFF). The wavelet-transformed Te K-edge EXAFS was analyzed using the HAMA code developed by H. Funke and M. Chukalina.[42] 2025-type coin cells with an open hole (sealed by Kapton tape) in the middle to allow X-ray incidence were used for operando tests. A titanium foil with a hole was placed between the coin cell case and cathode to avoid corrosion. The TeG electrode was fabricated using the same method above with a higher mass loading of Te (≈3 mg cm^{-2}). The Biologic VMP3 potentiostat with eight channels from PETRA III beamline P02.1 was utilized to perform operando measurements.

Molecular Dynamics Simulations: The simulation box had a cube shape with a length of 50 Å. Parameters of the atomic models of Zn^{2+} and Cl^{-} were based on the amber99sb-ildn force field.[43] 3D periodic boundary conditions were used. For water molecules, the four-site water model TIP4P/Ew was used.[44] The cut-off distance of nonbonded interactions was 10 Å, and the long-range electrostatic interactions were calculated by the particle-mesh Ewald method.[45] Initial structures for simulation were constructed by the Packmol software package.[46] The ions and solvent molecules were randomly placed in a simulated box to provide homogeneous structures. Before the dynamics simulation, the conjugated gradient method was used to pre-equalize the system to eliminate the excessive stress in initial structures. After pre-equilibrium, an NPT ensemble was used to equilibrate the system under room conditions (298.15 K and 1 atm) for 2 ns. Then, a 10 ns production simulation in the NVT ensemble at 298.15 K was carried out for data collection. Temperature and pressure coupling were performed using a v-rescale thermostat and Berendsen barostat.[47] All simulations were carried out by using the GROMACS 2019.4 software package.[48] All visualization structures were provided by VMD 1.9.3 software.[49]

Radial distribution functions (RDF) $g(r)_{A-B}$ were calculated by Equation (8), where ρ_b was the density of type-B atoms averaged over all spheres around type-A atoms. The coordination number was determined by the number of particles in the first solvation shell of the ion. Therefore, the integral value of the radial distribution function at the first valley was the average coordination number. The corresponding integral number was calculated by Equation (9), where ρ_N was the average number density of coordination atoms.[50]

$$g(r)_{A-B} = \frac{1}{\rho_b}\frac{1}{N_A}\sum_{i=1}^{N_A}\sum_{J=1}^{N_B}\frac{\delta\left(r_{ij}\right)-r}{4\pi r^2} \tag{8}$$

$$N(r) = 4\pi\,\rho_N\int_0^r r^2 g(r)\,dr \tag{9}$$

Supporting Information

Supporting Information is available from the Wiley Online Library or from the author.

Acknowledgements

This work was financially supported by the European Union's Horizon 2020 research and innovation programme (GrapheneCore3 881603, LIGHT-CAP 101017821), M-ERA.NET and Sächsisches Staatsministerium für Wissenschaft und Kunst (HYSUCAP 100478697), and the German Research Foundation (DFG) within the Cluster of Excellence, CRC 1415 (Grant No. 417590517). C.N. and A.T. acknowledge financial support by the Deutsche Forschungsgemeinschaft (DFG) within the CRC-TRR 234 "CataLight" projects B07 and Z02. J.D., Y.Z., X.C., D.L., and J.Z. thank the China Scholarship Council for financial support. The authors acknowledge the use of the facilities in the Dresden Center for Nanoanalysis (DCN) at Technische Universität Dresden, the GWK support for providing computing time through the Center for Information Services and High-Performance Computing (ZIH) at TU Dresden, beam time allocation at beamline P65 at the PETRA III synchrotron (DESY, Hamburg, Germany), and beamline BL22 at ALBA synchrotron (Barcelona, Spain). The authors also thank Panpan Zhao and Wenbo Zhang for the TEM characterization.

Open access funding enabled and organized by Projekt DEAL.

Conflict of Interest

The authors declare no conflict of interest.

Data Availability Statement

The data that support the findings of this study are available from the corresponding author upon reasonable request.

Keywords

aqueous zinc batteries, conversion electrochemistry, redox-amphoteric, tellurium

Received: December 13, 2023
Published online:

[1] a) D. Larcher, J. M. Tarascon, *Nat. Chem.* **2015**, *7*, 19; b) Y. Liang, Y. Yao, *Nat. Rev. Mater.* **2023**, *8*, 109.

[2] a) N. Zhang, X. Chen, M. Yu, Z. Niu, F. Cheng, J. Chen, *Chem. Soc. Rev.* **2020**, *49*, 4203; b) F. Wang, J. Tseng, Z. Liu, P. Zhang, G. Wang, G. Chen, W. Wu, M. Yu, Y. Wu, X. Feng, *Adv. Mater.* **2020**, *32*, 2000287; c) H. Zhang, W. Wu, Q. Liu, F. Yang, X. Shi, X. Liu, M. Yu, X. Lu, *Angew. Chem., Int. Ed.* **2021**, *60*, 896.

[3] a) F. Wang, O. Borodin, T. Gao, X. Fan, W. Sun, F. Han, A. Faraone, J. A. Dura, K. Xu, C. Wang, *Nat. Mater.* **2018**, *17*, 543; b) Q. Zhang, J. Luan, Y. Tang, X. Ji, H. Wang, *Angew. Chem., Int. Ed.* **2020**, *59*, 13180; c) M. Yu, N. Chandrasekhar, R. K. M. Raghupathy, K. H. Ly, H. Zhang, E. Dmitrieva, C. Liang, X. Lu, T. D. Kuhne, H. Mirhosseini, I. M. Weidinger, X. Feng, *J. Am. Chem. Soc.* **2020**, *142*, 19570.

[4] S. B. Wang, Q. Ran, R. Q. Yao, H. Shi, Z. Wen, M. Zhao, X. Y. Lang, Q. Jiang, *Nat. Commun.* **2020**, *11*, 1634.

[5] a) Z. Tao, Y. Zhu, Z. Zhou, A. Wang, Y. Tan, Z. Chen, M. Yu, Y. Yang, *Small* **2022**, *18*, 2107971; b) L. Cao, D. Li, T. Pollard, T. Deng, B. Zhang, C. Yang, L. Chen, J. Vatamanu, E. Hu, M. J. Hourwitz, *Nat. Nanotechnol.* **2021**, *16*, 902.

[6] a) L. Cao, D. Li, F. A. Soto, V. Ponce, B. Zhang, L. Ma, T. Deng, J. M. Seminario, E. Hu, X. Q. Yang, *Angew. Chem., Int. Ed.* **2021**, *60*, 18845; b) H. Jiang, L. Tang, Y. Fu, S. Wang, S. K. Sandstrom, A. M. Scida, G. Li, D. Hoang, J. J. Hong, N.-C. Chiu, K. C. Stylianou, W. F. Stickle, D. Wang, J. Li, P. A. Greaney, C. Fang, X. Ji, *Nat. Sustainability* **2023**, *6*, 806.

[7] a) H. Qiu, X. Du, J. Zhao, Y. Wang, J. Ju, Z. Chen, Z. Hu, D. Yan, X. Zhou, G. Cui, *Nat. Commun.* **2019**, *10*, 5374; b) L. Ma, M. A. Schroeder, O. Borodin, T. P. Pollard, M. S. Ding, C. Wang, K. Xu, *Nat. Energy* **2020**, *5*, 743.

[8] P. Yu, Y. Zeng, H. Zhang, M. Yu, Y. Tong, X. Lu, *Small* **2019**, *15*, 1804760.
[9] a) Y. Yuan, R. Sharpe, K. He, C. Li, M. T. Saray, T. Liu, W. Yao, M. Cheng, H. Jin, S. Wang, K. Amine, R. Shahbazian-Yassar, M. S. Islam, J. Lu, *Nat. Sustainability* **2022**, *5*, 890; b) H. Pan, Y. Shao, P. Yan, Y. Cheng, K. S. Han, Z. Nie, C. Wang, J. Yang, X. Li, P. Bhattacharya, K. T. Mueller, J. Liu, *Nat. Energy* **2016**, *1*, 16039; c) B. Sambandam, V. Mathew, S. Kim, S. Lee, S. Kim, J. Y. Hwang, H. J. Fan, J. Kim, *Chem* **2022**, *8*, 924.
[10] a) L. L. Wang, K. W. Huang, J. T. Chen, J. R. Zheng, *Sci. Adv.* **2019**, *5*, eaax4279; b) K. Y. Zhu, W. K. Jiang, Z. Wang, W. J. Li, W. L. Xie, H. M. Yang, W. S. Yang, *Angew. Chem., Int. Ed.* **2022**, *62*, 202213368; c) J. Ding, Z. Du, B. Li, L. Wang, S. Wang, Y. Gong, S. Yang, *Adv. Mater.* **2019**, *31*, 1904369.
[11] Z. Song, L. Miao, H. Duan, L. Ruhlmann, Y. Lv, D. Zhu, L. Li, L. Gan, M. Liu, *Angew. Chem., Int. Ed.* **2022**, *61*, 202208821.
[12] Q. Zhao, W. W. Huang, Z. Q. Luo, L. J. Liu, Y. Lu, Y. X. Li, L. Li, J. Y. Hu, H. Ma, J. Chen, *Sci. Adv.* **2018**, *4*, eaao1761.
[13] Y. Zhao, D. Wang, X. Li, Q. Yang, Y. Guo, F. Mo, Q. Li, C. Peng, H. Li, C. Zhi, *Adv. Mater.* **2020**, *32*, 2003070.
[14] Z. Chen, F. Mo, T. Wang, Q. Yang, Z. Huang, D. Wang, G. Liang, A. Chen, Q. Li, Y. Guo, X. Li, J. Fan, C. Zhi, *Energy Environ. Sci.* **2021**, *14*, 2441.
[15] Z. Chen, Q. Yang, F. Mo, N. Li, G. Liang, X. Li, Z. Huang, D. Wang, W. Huang, J. Fan, C. Zhi, *Adv. Mater.* **2020**, *32*, 2001469.
[16] C. R. Princival, M. Archilha, A. A. Dos Santos, M. P. Franco, A. A. C. Braga, A. F. Rodrigues-Oliveira, T. C. Correra, R. Cunha, J. V. Comasseto, *ACS Omega* **2017**, *2*, 4431.
[17] Z. Chen, S. Wang, Z. Wei, Y. Wang, Z. Wu, Y. Hou, J. Zhu, Y. Wang, G. Liang, Z. Huang, A. Chen, D. Wang, C. Zhi, *J. Am. Chem. Soc.* **2023**, *145*, 20521.
[18] X. Ji, *eScience* **2021**, *1*, 99.
[19] C. Zhang, J. Holoubek, X. Wu, A. Daniyar, L. Zhu, C. Chen, D. P. Leonard, I. A. Rodríguez-Pérez, J.-X. Jiang, C. Fang, *Chem. Commun.* **2018**, *54*, 14097.
[20] M. H. Alfaruqi, V. Mathew, J. Gim, S. Kim, J. Song, J. P. Baboo, S. H. Choi, J. Kim, *Chem. Mater.* **2015**, *27*, 3609.
[21] N. Zhang, F. Cheng, J. Liu, L. Wang, X. Long, X. Liu, F. Li, J. Chen, *Nat. Commun.* **2017**, *8*, 405.
[22] B. Wu, G. Zhang, M. Yan, T. Xiong, P. He, L. He, X. Xu, L. Mai, *Small* **2018**, *14*, 1703850.
[23] G. Fang, C. Zhu, M. Chen, J. Zhou, B. Tang, X. Cao, X. Zheng, A. Pan, S. Liang, *Adv. Funct. Mater.* **2019**, *29*, 1808375.
[24] N. Zhang, Y. Dong, M. Jia, X. Bian, Y. Wang, M. Qiu, J. Xu, Y. Liu, L. Jiao, F. Cheng, *ACS Energy Lett.* **2018**, *3*, 1366.
[25] J. Ding, Z. Du, L. Gu, B. Li, L. Wang, S. Wang, Y. Gong, S. Yang, *Adv. Mater.* **2018**, *30*, 1800762.
[26] D. Kundu, S. Hosseini Vajargah, L. Wan, B. Adams, D. Prendergast, L. F. Nazar, *Energy Environ. Sci.* **2018**, *11*, 881.
[27] F. Wan, L. Zhang, X. Wang, S. Bi, Z. Niu, J. Chen, *Adv. Funct. Mater.* **2018**, *28*, 1804975.
[28] Z. Guo, Y. Ma, X. Dong, J. Huang, Y. Wang, Y. Xia, *Angew. Chem., Int. Ed.* **2018**, *57*, 11737.
[29] M. A. Khayum, M. Ghosh, V. Vijayakumar, A. Halder, M. Nurhuda, S. Kumar, M. Addicoat, S. Kurungot, R. Banerjee, *Chem. Sci.* **2019**, *10*, 8889.
[30] G. Li, Z. Yang, Y. Jiang, C. Jin, W. Huang, X. Ding, Y. Huang, *Nano Energy* **2016**, *25*, 211.
[31] F. Wang, E. Hu, W. Sun, T. Gao, X. Ji, X. Fan, F. Han, X.-Q. Yang, K. Xu, C. Wang, *Energy Environ. Sci.* **2018**, *11*, 3168.
[32] F. Wan, Y. Zhang, L. Zhang, D. Liu, C. Wang, L. Song, Z. Niu, J. Chen, *Angew. Chem., Int. Ed.* **2019**, *58*, 7062.
[33] Z. Liu, G. Pulletikurthi, F. Endres, *ACS Appl. Mater. Interfaces* **2016**, *8*, 12158.
[34] R. Trocoli, F. L.a Mantia, *ChemSusChem* **2015**, *8*, 481.
[35] L. Zhang, L. Chen, X. Zhou, Z. Liu, *Adv. Energy Mater.* **2015**, *5*, 1400930.
[36] L. Ma, S. Chen, C. Long, X. Li, Y. Zhao, Z. Liu, Z. Huang, B. Dong, J. A. Zapien, C. Zhi, *Adv. Energy Mater.* **2019**, *9*, 1902446.
[37] L. Li, F. Meng, S. Jin, *Nano Lett.* **2012**, *12*, 6030.
[38] S. Cai, X. Chu, C. Liu, H. Lai, H. Chen, Y. Jiang, F. Guo, Z. Xu, C. Wang, C. Gao, *Adv. Mater.* **2021**, *33*, 2007470.
[39] Z. Chen, Q. Yang, D. Wang, A. Chen, X. Li, Z. Huang, G. Liang, Y. Wang, C. Zhi, *ACS Nano* **2022**, *16*, 5349.
[40] B. Ravel, M. Newville, *J. Synchrotron Radiat.* **2005**, *12*, 537.
[41] M. Newville, *J. Synchrotron Radiat.* **2001**, *8*, 96.
[42] H. Funke, A. C. Scheinost, M. Chukalina, *Phys. Rev. B* **2005**, *71*, 094110.
[43] K. Lindorff-Larsen, S. Piana, K. Palmo, P. Maragakis, J. L. Klepeis, R. O. Dror, D. E. Shaw, *Proteins* **2010**, *78*, 1950.
[44] H. W. Horn, W. C. Swope, J. W. Pitera, J. D. Madura, T. J. Dick, G. L. Hura, T. Head-Gordon, *J. Chem. Phys.* **2004**, *120*, 9665.
[45] T. Darden, D. York, L. Pedersen, *J. Chem. Phys.* **1993**, *98*, 10089.
[46] L. Martínez, R. Andrade, E. G. Birgin, J. M. Martínez, *J. Comput. Chem.* **2009**, *30*, 2157.
[47] a) G. Bussi, D. Donadio, M. Parrinello, *J. Chem. Phys.* **2007**, *126*, 014101; b) H. J. Berendsen, J. v. Postma, W. F. Van Gunsteren, A. DiNola, J. R. Haak, *J. Chem. Phys.* **1984**, *81*, 3684.
[48] M. J. Abraham, T. Murtola, R. Schulz, S. Páll, J. C. Smith, B. Hess, E. Lindahl, *SoftwareX* **2015**, *1*, 19.
[49] W. Humphrey, A. Dalke, K. Schulten, *J. Mol. Graphics* **1996**, *14*, 33.
[50] a) Y. Liu, H. Lu, Y. Wu, T. Hu, Q. Li, *J. Chem. Phys.* **2010**, *132*, 124503; b) S. Cai, X. Chu, C. Liu, H. Lai, H. Chen, Y. Jiang, F. Guo, Z. Xu, C. Wang, C. Gao, *Adv. Mater.* **2021**, *33*, 2007470.